AGU PUBLICATIONS

Geophysical Research Letters

RESEARCH LETTER
10.1002/2016GL070842

Special Section:
The Arctic: An AGU Joint Special Collection

Tundra photosynthesis captured by satellite-observed solar-induced chlorophyll fluorescence

K. A. Luus[1], R. Commane[2], N. C. Parazoo[3], J. Benmergui[2], E. S. Euskirchen[4], C. Frankenberg[5], J. Joiner[6], J. Lindaas[2,7], C. E. Miller[3], W. C. Oechel[8,9], D. Zona[8,10], S. Wofsy[2], and J. C. Lin[11]

[1]Centre for Applied Data Analytics Research, Dublin, Ireland, [2]John A. Paulson School of Engineering and Applied Sciences, Harvard University, Cambridge, Massachusetts, USA, [3]Jet Propulsion Laboratory, Pasadena, California, USA, [4]Institute of Arctic Biology, University of Alaska Fairbanks, Fairbanks, Alaska, USA, [5]Environmental Science and Engineering, California Institute of Technology, Pasadena, California, USA, [6]NASA Goddard Space Flight Center, Greenbelt, Maryland, USA, [7]Department of Atmospheric Science, Colorado State University, Fort Collins, Colorado, USA, [8]Department of Biology, San Diego State University, San Diego, California, USA, [9]College of Life and Environmental Sciences, University of Exeter, Exeter, UK, [10]Department of Animal and Plant Sciences, University of Sheffield, Sheffield, UK, [11]Department of Atmospheric Sciences, University of Utah, Salt Lake, Utah, USA

Abstract Accurately quantifying the timing and magnitude of respiration and photosynthesis by high-latitude ecosystems is important for understanding how a warming climate influences global carbon cycling. Data-driven estimates of photosynthesis across Arctic regions often rely on satellite-derived enhanced vegetation index (EVI); we find that satellite observations of solar-induced chlorophyll fluorescence (SIF) provide a more direct proxy for photosynthesis. We model Alaskan tundra CO_2 cycling (2012–2014) according to temperature and shortwave radiation and alternately input EVI or SIF to prescribe the annual seasonal cycle of photosynthesis. We find that EVI-based seasonality indicates spring "green-up" to occur 9 days prior to SIF-based estimates, and that SIF-based estimates agree with aircraft and tower measurements of CO_2. Adopting SIF, instead of EVI, for modeling the seasonal cycle of tundra photosynthesis can result in more accurate estimates of growing season duration and net carbon uptake by arctic vegetation.

Key Points:
- Alaskan tundra has a shorter growing season and less net carbon uptake than estimated using satellite-derived vegetation indices
- Comparisons against site and aircraft CO_2 observations indicate that solar-induced fluorescence (SIF) captures tundra photosynthesis
- SIF-driven modeling of tundra photosynthesis enables improved accuracy and understanding of the carbon-climate system

Supporting Information:
- Supporting Information S1

Correspondence to:
K. A. Luus,
kristina.luus@gmail.com

Citation:
Luus, K. A., et al. (2017), Tundra photosynthesis captured by satellite-observed solar-induced chlorophyll fluorescence, *Geophys. Res. Lett.*, *44*, 1564–1573, doi:10.1002/2016GL070842.

Received 14 AUG 2016
Accepted 12 JAN 2017
Accepted article online 16 JAN 2017
Published online 4 FEB 2017

1. Introduction

Land-atmosphere CO_2 exchange can only be continuously measured at small scales (<1 km^2), and CO_2 concentrations measured by towers and aircraft are spatially and temporally limited. Accurate, fine-resolution model estimates of net ecosystem CO_2 exchange (NEE) across large regions are therefore needed in order to gain insight into how carbon cycling by high-latitude ecosystems influences atmospheric concentrations of CO_2 and the global climate system.

Vegetation influences on rates of photosynthesis (e.g., phenology, biomass, and leaf area) are typically inferred at regional scales using indices derived from satellite-observed visible and infrared reflectance, such as the normalized difference vegetation index (NDVI) and enhanced vegetation index (EVI) [*Barichivich et al.*, 2013; *Wang et al.*, 2015]. These indices are calculated as normalized ratios of visible and infrared reflectance and rely on the tendency for vegetation chlorophyll to absorb visible (0.4–0.7 μm) radiation and mesophyll to reflect near-infrared (0.7–1.1 μm) radiation. Larger EVI and NDVI values are indicative of denser or greener leaf cover [*Wang et al.*, 2002; *Sims et al.*, 2006], which can be interpreted as greater photosynthetic capacity.

Passive solar-induced chlorophyll fluorescence (SIF) provides a more direct proxy for photosynthesis [*Yang et al.*, 2015] independent of ancillary information or modeling steps and can be acquired from ground- and satellite-based observations [*Frankenberg et al.*, 2014]. SIF occurs as a direct result of light absorption by the chlorophyll complex during photosynthesis [*Porcar-Castell et al.*, 2014].

Photosynthesis is therefore directly correlated with SIF [*Frankenberg et al.*, 2011a], whereas EVI is associated with the capacity of the land surface for photosynthesis. EVI is more susceptible to being confounded with nonvegetated land surface properties than SIF. Unlike SIF, EVI has been observed to remain elevated (>0), throughout most of the Arctic snow season (Figure S2 in the supporting information), and to increase

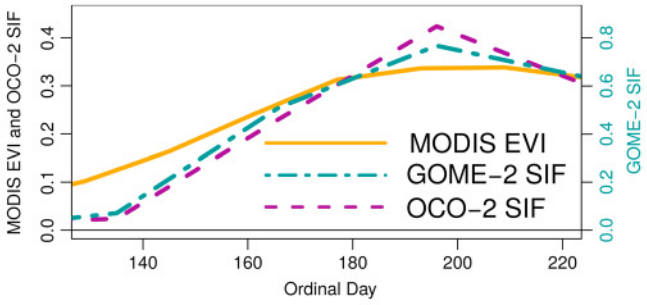

Figure 1. Spatially averaged 2014 seasonal cycle of MODIS EVI, OCO-2 SIF/cos(solar zenith angle, SZA), and GOME-2 SIF/cos(SZA) across Alaskan tundra.

during the time period over which vegetation is revealed through snowmelt. Conversely, SIF remains near zero throughout the nongrowing season and increases in response to photosynthesis (Figure 1). Through comparisons against aircraft and tower measurements of CO_2, we show here that more realistic model estimates of tundra photosynthesis can be generated when the seasonal cycle is prescribed using SIF rather than EVI.

1.1. Overview

We present satellite-data-driven estimates of Alaskan tundra NEE (3-hourly, 0.17° × 0.25°, 2012–2014) using Polar Vegetation Photosynthesis and Respiration Model (PolarVPRM) [*Luus and Lin*, 2015], a low dimensional, spatially and temporally resolved model developed according to empirical associations between site-scale meteorology and NEE. PolarVPRM-EVI has previously been applied to estimate Alaskan [*Karion et al.*, 2016] and northern Canadian [*Luus and Lin*, 2015] NEE.

We generate model estimates of Alaskan NEE and allow the seasonal cycle of photosynthesis to alternately be driven by EVI or SIF. We then confront EVI-driven and SIF-driven estimates of Alaskan NEE (2012–2014) across tundra-dominated (>80% tundra) regions with measurements of NEE from established eddy covariance sites (Table 1 and Figures 2 and S1) and observations of regional-scale CO_2 fluxes optimized from NASA's CARVE (Carbon in the Arctic Reservoirs Vulnerability Experiment) airborne CO_2 observations [*Miller and Dinardo*, 2012].

We find that PolarVPRM-SIF is better able to capture the timing and duration of the tundra growing season (time period over which mean weekly NEE<0) than PolarVPRM-EVI. PolarVPRM-EVI overestimates growing season length, despite the application of strategies to reduce spring and fall EVI, and the inclusion of scaling factors to reduce PolarVPRM-EVI photosynthesis at the start and end of the growing season (when EVI<50% annual EVI). PolarVPRM-SIF provides improved accuracy in regional estimates of the Alaskan carbon balance (Figure S5).

2. Methods

Methods applied to (1) observe site-scale CO_2 fluxes, (2) estimate duration of photosynthesis regionally from EVI and SIF, (3) generate regional model estimates of net ecosystem CO_2 exchange, and (4) calculate regional CO_2 fluxes from CARVE CO_2 observations are described below.

2.1. Site-Scale CO_2 Observations

Measurements of net ecosystem CO_2 exchange (NEE) were obtained from established Alaskan sites using eddy covariance towers, which were used for model calibration and validation. These sites include a sparsely forested thermokarst bog in central Alaska (Bonanza Creek) [*Euskirchen et al.*, 2014], two wet sedge sites

Table 1. Eddy Covariance Site Descriptions

Site	Latitude (°N)	Longitude (°W)	Vegetation	Reference
Atqasuk	70.470	157.409	Moist-wet sedge	*Kwon et al.* [2006]
Barrow	71.323	156.626	Wet sedge tundra	*Lipson et al.* [2012]
Bonanza	64.701	148.321	Thermokarst bog	*Euskirchen et al.* [2014]
Imnavait	68.606	149.304	Wet tussock/sedge tundra	*Euskirchen et al.* [2012]

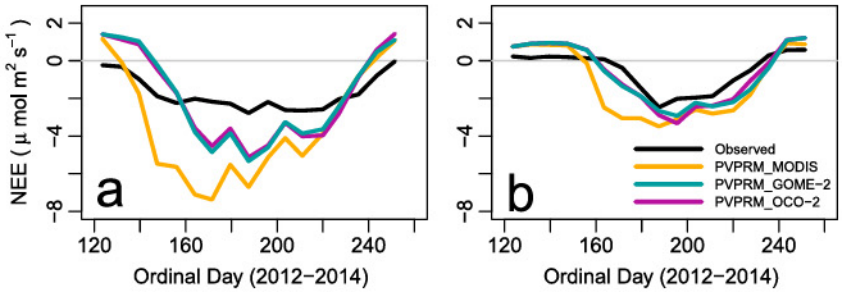

Figure 2. Time series (2012–2014) of mean eddy covariance NEE, EVI-based NEE, and SIF-based NEE at the (a) Bonanza Creek thermokarst bog and (b) Imnavait wet sedge sites, described in Table 1.

(Atqasuk and Barrow) [*Kwon et al.*, 2006; *Lipson et al.*, 2012], and a site containing wet sedge and tussock tundra (Imnavait) [*Euskirchen et al.*, 2012] (Table 1).

2.2. EVI and SIF

Moderate Resolution Imaging Spectroradiometer (MODIS) EVI observations (A. Huete et al., MODIS Vegetation Index (MOD13) Algorithm Theoretical Basis Document Version, Tech. Rep., 1999) were acquired from portions of the 16 day MOD13A1 data set with good QC flags and were smoothed using a loess filter, with spatial and temporal interpolation applied to remove missing values, and linear interpolation to ensure 3-hourly estimates for all pixels. Since MODIS EVI is reported according to the maximum value observed during a given time period, it was assumed that these maximum values would correspond to the final day of observations during green-up and to the first day of observations following the attainment of maximum annual EVI at each pixel. This approach was selected specifically to reduce EVI values in spring and autumn.

SIF was acquired across high-latitude regions using the Orbiting Carbon Observatory-2 (OCO-2) [*Frankenberg et al.*, 2011b] and Global Ozone Monitoring Experiment 2 (GOME-2) [*Joiner et al.*, 2013] instruments. Retrievals from GOME-2 on MetOp-A use channel 4, with 734–758 nm wavelengths and an ≈0.5 nm spectral resolution, were collected at a 1–2 day revisit time, and developed into a 0.5 × 0.5°, monthly, bias-corrected product (GOME2_F V26) by *Joiner et al.*, 2013 [2013, 2016].

Retrievals from OCO-2 were taken from the version 7 product using an algorithm described in *Frankenberg et al.* [2011b]. We used the average of nadir soundings at 757 nm and 771 nm bands with overpass of 2:15 P.M. local time, revisit time of a few weeks, and footprint of 1.3 × 2.25 km^2, where the 771 nm band was multiplied by 1.35 due to its smaller signal. Soundings were aggregated to monthly averages on a 0.17° × 0.25° grid using a minimum of five soundings per bin. A full year of OCO-2 SIF estimates was generated by combining SIF observations from 2014 (September–December) to 2015 (January–August). Monthly averages of OCO-2 SIF were generated using all available data from September 2014 to August 2015, and these monthly values were repeated for all years (2012–2014).

We included GOME-2 SIF and OCO-2 SIF at a monthly resolution because our preliminary findings indicated monthly SIF values to be reliable and adequate, in agreement with *Joiner et al.* [2014]. At the regional scale, median GOME-2 SIF and OCO-2 SIF values were separately calculated for each month and each vegetation class (Figure S4).

SIF values for each PolarVPRM pixel (0.17° × 0.25°) were then calculated as the weighted mean of SIF according to component vegetation fractions, and 3-hourly estimates of SIF were generated through linear interpolation of monthly values.

2.3. Estimating NEE

Estimates of NEE were generated for Alaska at a 3-hourly, 0.17° × 0.25° resolution using the Polar Vegetation Photosynthesis and Respiration Model (PolarVPRM) [*Luus and Lin*, 2015], a high-latitude version of VPRM [*Mahadevan et al.*, 2008]. PolarVPRM is a parametric fit to the classic hyperbolic form of the light response curve for an ecosystem of a defined vegetation type. Regional-scale estimates of NEE were acquired by calculating the weighted sum of gross ecosystem exchange (GEE= −1× GPP) and ecosystem respiration (R) at each pixel according to its fractional vegetation cover [*Walker et al.*, 2005; *Jung et al.*, 2006; *Luus et al.*, 2013a] (see Figure S4). For a full description, evaluation, and error attribution of PolarVPRM, refer to *Luus et al.* [2013b]; *Luus and Lin* [2015].

2.3.1. PolarVPRM Inputs

Meteorological inputs such as soil temperature at 0–10 cm (T_{soil}), air temperature at 2 m(T_{air}), and downward shortwave radiation (PAR = 1.98 · SW) were provided by the North American Regional Reanalysis [*Mesinger et al.*, 2006]. Land surface conditions were estimated from MODIS snow cover area (MOD10A2) [*Hall et al.*, 2002], and land surface water index was calculated from surface reflectance (MOD09A1).

We prescribe the seasonal cycle of vegetation green-up and senescence alternately by Moderate Resolution Imaging Spectroradiometer (MODIS) EVI (A. Huete, Tech. Rep., 1999), Global Ozone Monitoring Experiment 2 (GOME-2) SIF [*Joiner et al.*, 2013], or Orbiting Carbon Observatory-2 (OCO-2) SIF [*Frankenberg et al.*, 2014], where SIF is normalized by the cosine of the solar zenith angle.

2.3.2. PolarVPRM Equations

Ecosystem respiration was calculated as a function of air (growing season) and soil (snow season) temperature depending on MODIS-derived snow cover area, using a formulation that maximizes effective capture of sub-nivean and growing season drivers of Arctic respiration [*Luus et al.*, 2013c], including soil freeze-thaw cycles (equation(3)). GEE was calculated according to air temperature at 2 m (T_{air}) and photosynthetically active radiation, such that photosynthesis (GEE) is greatest when conditions are warm and sunny. The seasonal cycle of GEE was driven alternately by MODIS EVI (equation (1)) and SIF (equation (2)).

$$\mathrm{GEE} = \lambda \cdot \mathrm{EVI} \cdot T_{\mathrm{scale}} \cdot P_{\mathrm{scale}} \cdot \frac{1}{1 + \frac{\mathrm{PAR}}{\mathrm{PAR}_0}} \cdot \mathrm{PAR}. \tag{1}$$

$$\mathrm{GEE} = \lambda \cdot T_{\mathrm{scale}} \cdot \frac{\mathrm{SIF}}{\cos(\mathrm{SZA})} \cdot \frac{1}{1 + \frac{\mathrm{PAR}}{\mathrm{PAR}_0}} \cdot \mathrm{PAR}. \tag{2}$$

$$R = \begin{cases} \alpha_{\mathrm{grow}} \cdot T_{\mathrm{air}} + \beta_{\mathrm{grow}} & : \text{snow cover} < 50\% \\ \alpha_{\mathrm{snow}} \cdot T_{\mathrm{soil}} + \beta_{\mathrm{snow}} & : \text{snow cover} \geq 50\% \end{cases}. \tag{3}$$

2.3.3. PolarVPRM Parameters

All parameters were calculated empirically so as to capture associations between site meteorology and eddy covariance NEE. The model parameters PAR_0 and λ (Table 2) refer to the half-saturation value of PAR and light-use efficiency at low light levels, respectively. PAR_0 was first calculated from PAR and GPP using `nls` non-linear curve fitting in *R* [*R Core Team*, 2013], and λ was then calculated as the slope of the linear regression of observed and modeled 3-hourly GEE (with $\lambda = 1$, and intercept = 0) at three eddy covariance sites (Table 1). Estimates across forested regions in interior Alaska were generated using PAR_0 and λ values in *Mahadevan et al.* [2008]. Linear regression was used to determine the slope (α) and intercept (β) of the associations between nighttime NEE (respiration) and soil/air temperature, using only values for which PAR indicated night and NEE>0.

SIF-based models used identical PAR_0 values as EVI-based models, since PAR was unchanged. However, to account for the different magnitudes of OCO-2 SIF and GOME-2 SIF relative to MODIS EVI, λ values were multiplied by a scaling factor describing the slope of EVI-based versus SIF-based GEE at calibration eddy covariance sites. In this way, it was ensured that differences in EVI-based and SIF-based outputs would arise from inputs alone. PolarVPRM-EVI NEE additionally benefits from having corrections implemented so as to reduce the length of the modeled growing season: inclusion of scalars described in section 2.3.4 (P_{scale}, T_{scale}) and preprocessing of EVI as described in section 2.2.

2.3.4. PolarVPRM Scalars

$$T_{\mathrm{scale}} = \frac{(T_{\mathrm{air}} - T_{\mathrm{min}})(T_{\mathrm{air}} - T_{\mathrm{max}})}{(T_{\mathrm{air}} - T_{\mathrm{min}})(T_{\mathrm{air}} - T_{\mathrm{max}}) - (T_{\mathrm{air}} - T_{\mathrm{opt}})^2}. \tag{4}$$

The temperature scalar (equation (4)) is calculated according to minimum ($T_{\mathrm{min}} = 0°\mathrm{C}$) and maximum ($T_{\mathrm{max}} = 40°\mathrm{C}$) temperature thresholds for photosynthesis, as well as an optimal temperature (T_{opt}). T_{opt} was set according to values in literature [*Tieszen*, 1973; *Chapin*, 1983; *O'Sullivan et al.*, 2016] rather than being optimized in order to avoid parameter instability arising from correlations between temperature and light-use parameters [*Mahadevan et al.*, 2008] (Table 2).

Table 2. Parameter Values for All Models (MODIS EVI, GOME-2 SIF, and OCO-2 SIF)[a]

Parameter	Model	Evergreen Forest	Deciduous Forest	Mixed Forest	Shrubs	Shrub Tundra	Graminoid Tundra	Wetland
λ	MODIS	0.234	0.127	0.123	0.122	0.040	0.030	0.149
λ	GOME-2	0.065	0.040	0.035	0.038	0.020	0.014	0.072
λ	OCO-2	0.117	0.061	0.064	0.064	0.046	0.028	0.160
PAR_0	All	262	570	629	321	241	241	241
T_{opt}	All	20	20	20	20	15	15	10

[a] $T_{min} = 0°C$ and $T_{max} = 40°C$ for all models and vegetation classes (Figure S4).

In EVI-driven PolarVPRM, T_{scale} (equation (4)) ensures that GEE=0 during the snow season (when $T_{air} < 0°C$) and reduces GPP at the start and end of the snow season, when air temperatures approach freezing. In contrast, SIF GPP estimates showed little sensitivity to T_{scale} and did not require any artificial suppression of nongrowing-season photosynthesis. Final estimates of GPP by both versions of PolarVPRM include T_{scale} so as to capture midgrowing season reductions in photosynthesis due to heat stress [*O'Sullivan et al.*, 2016] in both models and to reduce cold-season and shoulder-season GPP overestimates by PolarVPRM-EVI.

$$P_{scale} = \frac{1 + \mathrm{LSWI}}{2}. \tag{5}$$

The phenology scalar, P_{scale}, is prescribed in the EVI version of VPRM and PolarVPRM to reduce photosynthesis when EVI is at <50% of maximum annual pixel-specific EVI, so as to reduce overestimates of photosynthesis in spring and fall (equation (5)). This was applied in the EVI version of PolarVPRM to reduce errors arising from elevated (>0) EVI before and after the growing season, but was not needed in the SIF version of PolarVPRM. In short, the two scalar terms, T_{scale} and P_{scale}, both reduce overestimates of GPP by PolarVPRM-EVI, especially at the start and end of the growing season.

2.4. Regional-Scale CO_2 Observations

CO_2 concentrations were measured during Carbon in Arctic Reservoirs Vulnerability Experiment (CARVE) flight campaigns, which were conducted over Alaska throughout the 2012–2014 growing seasons. The NASA C-23B (N430NA) aircraft was based in Fairbanks, Alaska, USA, and flights sampled the region between 55°–72°N and 165°–138°W. CO_2, CH_4, and CO were measured using two independent cavity ringdown spectrometers: one operated wet (G1301-m in 2012 and G2401-m from 2013 onward) [*Karion et al.*, 2013] and one dry (G2401-m) [*Chang et al.*, 2014]. Each analyzer was calibrated throughout the flights, with gap filling to ensure a continuous 5 s time series.

Airborne CO_2 concentrations (ppm) were modeled to gain insight into the magnitudes and locations of CO_2 fluxes (μmol m^{-2} s^{-1}) giving rise to observed CO_2 concentrations. First, modeled column CO_2 concentrations were calculated for altitude profiles within each flight using pWRF-STILT (polar variant of Weather Forecasting and Research-Stochastic Time Inverted Lagrangian Transport model) [*Henderson et al.*, 2015; *Lin et al.*, 2003] mapping of land surface influences on mean 3-hourly CO_2 concentrations. These results are provided on a 0.5°×0.5° grid that represents the response of each receptor to a unit emission of CO_2 at each grid square (in $\frac{\mu mol}{mol} / \frac{\mu mol}{m^2 s}$). The column integral represents the mass loading of regional emissions on the atmosphere from the surface to the top of the mixed layer. The column enhancement of CO_2 mole fractions combines all fluxes to give an integrated signal used in the column analysis. Episodic or point sources of CO_2 will have little influence on this integrated signal.

Alaskan NEE was calculated from these CARVE CO_2 data sets. Mean monthly additive fluxes (δF, in $\frac{\mu mol}{m^2 s}$) were calculated as the difference between the integrated column enhancement of the observed and modeled CO_2 for each profile and were calculated separately using PolarVPRM-EVI and PolarVPRM-SIF. CARVE-constrained estimates of NEE were then generated by adding δF to the mean spatially averaged NEE from PolarVPRM-EVI and PolarVPRM-SIF.

CARVE NEE fluxes are a result of mass balance considerations based upon tracer variations in the atmospheric planetary boundary layer, which is the most direct means we have possible to observe and quantify regional carbon fluxes. The mean of the 273 CARVE column profiles used for this approach is shown in Figure 3,

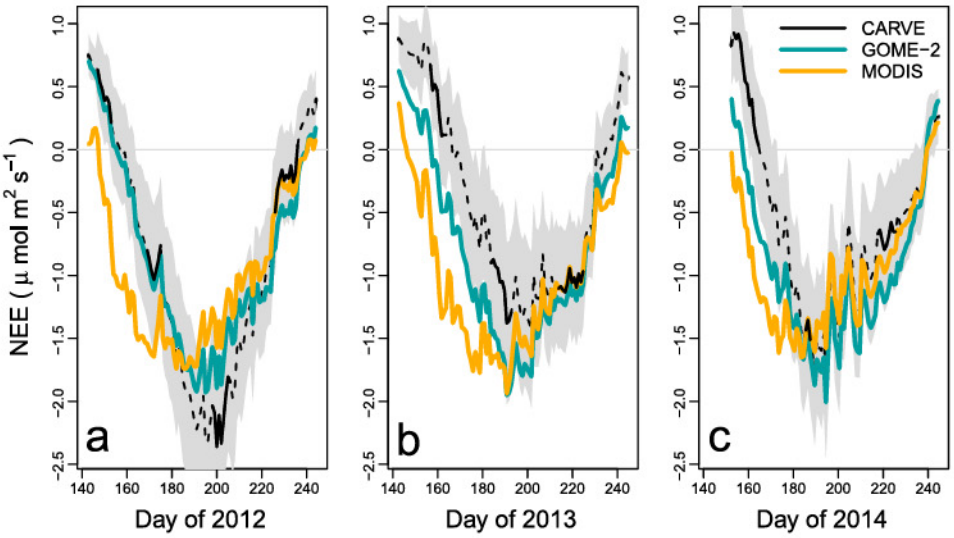

Figure 3. Spatially averaged Alaskan tundra NEE simulated using MODIS EVI and GOME-2 SIF, and CARVE-optimized NEE across Alaskan tundra in (a) 2012, (b) 2013, and (c) 2014. In all plots, the time series of mean CARVE-optimized NEE from 273 column profiles is indicated with a solid black line, interpolated NEE is indicated with a dotted line, and the standard deviation of the additive flux from CARVE column profiles is indicated in grey.

along with the standard deviation of the additive flux from each of these profiles, to indicate quantitatively the uncertainty of CARVE fluxes. For additional details regarding the approach used to examine CARVE CO_2 observations, please refer to *Henderson et al.* [2015].

3. Results

3.1. Site Scale

We confronted both PolarVPRM-EVI and PolarVPRM-SIF NEE with site-scale observations of NEE collected at four established Alaskan eddy covariance sites (2012–2014) (Table 1). PolarVPRM-EVI NEE overestimated the timing and magnitude of late winter photosynthesis at bog, sedge, and tussock tundra sites. Unlike SIF, EVI increased during late winter snowmelt (Figure 1) and remained elevated throughout the late snow season (Figure S2). Overall, growing season onset was better captured using PolarVPRM-SIF than PolarVPRM-EVI at tundra sites (Figure 2).

If the carbon uptake period is estimated from EVI, the start of the tundra growing season is therefore assumed to occur earlier than observed at the site scale. Since solar radiation is used to estimate photosynthesis, the coincident timing of the solar maximum and snowmelt-induced increases in EVI conspire to result in large overestimates of spring photosynthesis. Conversely, applying a SIF-based approach enables model estimates to capture the timing of peak photosynthesis (Figure 2).

3.2. Regional

A comparison of NEE modeled using SIF and EVI to CARVE-optimized NEE revealed a tendency for spring photosynthetic uptake to be overestimated when the seasonal cycle was prescribed using EVI (Figure 3). Evaluation of daily mean model NEE against daily mean CARVE NEE indicated that the SIF-based model had a root-mean-square error (RMSE) of 0.387 μmol m^{-2} s^{-1}, whereas the EVI-based model had an RMSE of 0.579 μmol m^{-2} s^{-1}. CARVE-optimized NEE indicated that the growing season (when weekly NEE<0) began on days 160, 167, and 161 in 2012, 2013, and 2014, respectively. Relative to CARVE data, EVI-based estimates of NEE indicated the growing season to begin 9, 20, and 16 days too early, whereas the SIF-based approach underestimated these dates by only 1, 9, and 8 days. This corresponds to biases of 15 days by PolarVPRM-EVI and 6 days by PolarVPRM-SIF.

GOME-2 SIF more accurately captures the seasonal cycle of tundra photosynthesis than MODIS EVI. Prescribing a seasonal cycle of photosynthesis using GOME-2 SIF rather than MODIS EVI resulted in improved agreement between modeled and observed NEE across Alaska's tundra-dominated regions. Overestimates

of tundra photosynthesis by EVI-driven models result in diminished accuracy in estimates of Alaska's carbon cycle (Figure S6), whereas SIF-driven estimates show reasonable agreement with CARVE observations across Alaska (Figure S5).

4. Discussion

4.1. SIF Captures Spring Photosynthetic Onset Better Than EVI

Whereas EVI represents the presence, quantity, or health of aboveground vegetation [*Wang et al.*, 2002; *Sims et al.*, 2006], from which photosynthetic capacity can be inferred, SIF occurs as a direct result of light absorption by the chlorophyll complex [*Yang et al.*, 2015; *Frankenberg et al.*, 2014; *Parazoo et al.*, 2013]. SIF is therefore more likely than EVI to capture the lag between initial spring snowmelt, start of growing season (NEE<0), and onset of high rates of canopy photosynthesis [*Joiner et al.*, 2014].

In snow-dominated regions, EVI can remain elevated (>0) throughout most of the snow season if canopy height exceeds snow depth or if influenced by nonvegetation land surface properties (Figure S2). In late winter, EVI rises quickly from a nonzero base value in response to the appearance of senescent vegetation revealed through snowmelt, and confounding changes over time in nonchlorophyll containing surface properties, rather than due to leaf-out or photosynthetic onset [*Fontana et al.*, 2008; *Jin and Eklundh*, 2014]. The combination of these errors in estimating the seasonal cycle of photosynthesis using EVI would be difficult to correct fully for across large, heterogeneous and cloudy region such as Alaska.

EVI-driven models can estimate photosynthesis to occur throughout the portion of the late snow season and early growing season where warm (>0°C) and sunny conditions prevail. The timing of snowmelt and photosynthesis may initially coincide when evergreen Arctic vegetation rapidly begins to photosynthesize during initial snowmelt while air temperatures and subnivean CO_2 concentrations are high [*Starr and Oberbauer*, 2003]. However, productivity has been observed to stall following snowmelt, and the rate of net CO_2 efflux has been observed to increase slightly when exposed to freeze-thaw cycles [*Larsen et al.*, 2007]. Without the insulating effect of a dry snowpack, vegetation is likely to be more vulnerable to cold air temperatures during and following snowmelt, which can cause damage and disproportionately hinder green-up, leaf-out, and photosynthetic onset [*Bokhorst et al.*, 2009]. Relying on EVI for modeling Arctic NEE can therefore result in overestimates of photosynthetic rates throughout the late snow season and early growing season.

4.2. Tundra NEE Is Better Captured by SIF Than EVI

SIF reliably captures the seasonal cycle of tundra photosynthesis, which is consistent with previous studies of non-Arctic ecosystems (i.e., savannas [*Pérez-Priego et al.*, 2015], rainforests [*Lee et al.*, 2013], forests [*Walther et al.*, 2015], and crops [*Guanter et al.*, 2014]). Establishing the utility of SIF for tundra regions provides further motivation for widespread application of a SIF-based approach to global carbon cycle modeling.

Using SIF, rather than EVI, to estimate tundra NEE enables closer agreement between modeled and observed NEE due mainly to differences in timing of growing season onset and the tendency for SIF to remain near 0 throughout the nongrowing season. Similar seasonal patterns in APAR relative to SIF have been observed in boreal forests [*Joiner et al.*, 2013], and we find similar patterns in Alaskan MODIS GPP (S. W. Running and M. Zhao, Daily GPP and Annual NPP (MOD17A2/A3) Products NASA Earth Observing System MODIS Land Algorithm, 2015) (Figure S6). Additionally, whereas PolarVPRM-EVI requires scalar terms to reduce shoulder-season photosynthesis and suppress cold-season photosynthesis, SIF provides more direct estimates of tundra's seasonal cycle and so can be included parsimoniously in models.

Arctic warming caused by climate change can both enable more carbon uptake by high-latitude vegetation due to a lengthening growing season [*Goetz et al.*, 2005; *Groendahl et al.*, 2007] and increase rates of carbon release from thawing permafrost [*Schuur et al.*, 2008]. Accurately monitoring the Arctic carbon balance is important due to the immense quantity (≈1700 Gt) of soil organic carbon [*Tarnocai et al.*, 2009] underlying Arctic regions, and positive feedbacks between climate warming and greenhouse gas emissions from permafrost [*Schuur et al.*, 2015]. Accurately characterizing net carbon uptake by tundra ecosystems at the regional scale and monitoring changes over time in growing season onset and length are therefore critically important.

4.3. SIF-Based Modeling of Tundra NEE

Satellite-data-driven estimates of tundra photosynthesis can be calculated empirically from meteorological observations and SIF, according to site-scale associations between NEE and meteorology. Accurate model

estimates of regional-scale carbon cycling rely on an appropriate model formulation, parameter fitting, selection of satellite indices, and processing of satellite inputs to the model.

In light of the similarity in estimates of tundra NEE generated from OCO-2 SIF and GOME-2 SIF, future work may focus on examining the potential to create a blended product that exploits GOME-2's longer data record and complete spatial coverage, and OCO-2's finer spatial resolution. Further reductions in uncertainty regarding global photosynthesis will likely also result from combining SIF observations from OCO-2 and GOME-2 with SIF retrieved by the TROPOspheric Monitoring Instrument (TROPOMI). TROPOMI will have a wide swath, high signal-to-noise ratio, fine spatial resolution in global composites (0.1°), and large number of clear-sky observations over land per day relative to existing products [*Guanter et al.*, 2015].

The results presented here also suggest strategies for improving the accuracy of process-based estimates of high-latitude CO_2 cycling. Regional estimates of CO_2 concentrations over time by 13 established process-based models were recently evaluated relative to atmospheric observations of CO_2 through the International Land Model Benchmarking Project [*Hoffman et al.*, 2015]. Findings indicated systematic springtime overestimates of net carbon uptake by vegetation across high-latitude northern regions (50–70°N), due in part to an overly early start to the growing season. Photosynthesis in these process-based models was simulated using strategies resembling both SIF-based [*Ball et al.*, 1987] and EVI-based [*Roberts et al.*, 2004] approaches. Overestimates of spring photosynthetic uptake in these models may occur when deciduous growth of photosynthetic tissues or evergreen recovery from cold hardening are simulated to occur faster than they actually do [*Bergh et al.*, 1998]. Improved accuracy in process-based modeling of Arctic carbon cycling could therefore potentially be attained by simulating lags between green-up and growing season onset using tundra-specific stress factors relating to vegetation photosynthetic capacity.

5. Conclusions

SIF captures the timing of spring green-up and seasonal cycle of photosynthesis across Alaskan tundra. EVI indicates tundra growing season onset to occur an average of 9 days sooner than SIF. EVI-driven estimates of Arctic NEE likely estimate growing season onset to occur too soon and may overestimate growing season duration (Figure S6).

Alaskan tundra carbon cycling can be accurately modeled using an empirical, data-driven approach integrating satellite observations of SIF, temperature, and shortwave radiation. Prescribing the seasonal cycle of photosynthesis according to SIF enables accurate modeling of tundra NEE relative to tower and aircraft CO_2 measurements (RMSE=0.39 μmol m^{-2} s^{-1}). Alaskan carbon budget estimates are biased toward too much uptake if growing season length is prescribed by EVI instead of SIF (Figure S5).

Using an SIF-based approach to estimate tundra canopy photosynthesis therefore provides improved understanding of the extent to which high-latitude regions are taking up and releasing carbon, and how this is changing over time. SIF-driven modeling of tundra photosynthesis enables improved constraints on the tundra carbon cycle and enhanced understanding of feedbacks between Arctic carbon cycling and climate change.

Acknowledgments
The authors wish to acknowledge contributions from the OCO-2 and GOME-2 teams. Funding from NSERC through a Postdoctoral Fellowship (KAL) is gratefully acknowledged. Some of the research described in this paper was performed for the Carbon in Arctic Reservoirs Vulnerability Experiment (CARVE), an Earth Ventures (EV-1) investigation, under contract with NASA. A portion of the research described in this paper was performed at the Jet Propulsion Laboratory, California Institute of Technology, under contract with the National Aeronautics and Space Administration. Data from Imnavait, Alaska, were provided by E. Euskirchen, C. Edgar, and M.S. Bret-Harte and collected through a grant from the National Science Foundation Collaborative Research on Carbon, Water, and Energy Balance of the Arctic Landscape at Flagship Observatories in Alaska and Siberia. Eddy covariance and meteorological observations from Barrow and Atqasuk were provided by W. Oechel, D. Zona, and the Global Change Research Group. Funding and support were provided by CARVE subcontract 1443296, under contract with NASA, and by the NASA grant, award NNX16AF94A, Arctic-Boreal Vulnerability Experiment (ABoVE) to W. Oechel and by Division of Polar Programs of the National Science Foundation (NSF) (award 1204263) to D. Zona. NCEP Reanalysis data were provided by the NOAA/OAR/ESRL PSD, Boulder, Colorado, USA, from their Web site at http://www.esrl.noaa.gov/psd/. The MODIS MOD13A1, MOD10A2, and MOD09A1 data products were retrieved from the online Data Pool, courtesy of the NASA Land Processes Distributed Active Archive Center (LP DAAC), USGS/Earth Resources Observation and Science (EROS) Center, Sioux Falls, South Dakota, https://lpdaac.usgs.gov/data_access/data_pool. MOD17A2 GPP was provided by the Numerical Terradynamic Simulation Group (NTSG) at the University of Montana. We wish to thank the Oak Ridge National Lab for hosting open access to all Alaskan PolarVPRM outputs presented here, which can be downloaded from *Luus and Lin* [2016].

References

Ball, J. T., I. E. Woodrow, and J. A. Berry (1987), A model predicting stomatal conductance and its contribution to the control of photosynthesis under different environmental conditions, in *Progress in Photosynthesis Research*, edited by J. Biggins, pp. 221–224, Springer, Netherlands.

Barichivich, J., K. R. Briffa, R. B. Myneni, T. J. Osborn, T. M. Melvin, P. Ciais, S. Piao, and C. Tucker (2013), Large-scale variations in the vegetation growing season and annual cycle of atmospheric CO_2 at high northern latitudes from 1950 to 2011, *Global Change Biol.*, *19*(10), 3167–3183.

Bergh, J., R. E. McMurtrie, and S. Linder (1998), Climatic factors controlling the productivity of Norway spruce: A model-based analysis, *For. Ecol. Manage.*, *110*(1), 127–139.

Bokhorst, S. F., J. W. Bjerke, H. Tømmervik, T. V. Callaghan, and G. K. Phoenix (2009), Winter warming events damage sub-Arctic vegetation: Consistent evidence from an experimental manipulation and a natural event, *J. Ecol.*, *97*(6), 1408–1415.

Chang, R. Y.-W., et al. (2014), Methane emissions from Alaska in 2012 from CARVE airborne observations, *Proc. Natl. Acad. Sci. U.S.A.*, *111*(47), 16,694–16,699.

Chapin, F., III (1983), Direct and indirect effects of temperature on Arctic plants, *Polar Biol.*, *2*(1), 47–52.

Euskirchen, E., M. S. Bret-Harte, G. Scott, C. Edgar, and G. R. Shaver (2012), Seasonal patterns of carbon dioxide and water fluxes in three representative tundra ecosystems in northern Alaska, *Ecosphere*, *3*(1), 4.

Euskirchen, E., C. Edgar, M. Turetsky, M. Waldrop, and J. Harden (2014), Differential response of carbon fluxes to climate in three peatland ecosystems that vary in the presence and stability of permafrost, *J. Geophys. Res. Biogeosci.*, *119*, 1576–1595, doi:10.1002/2014JG002683.

Fontana, F., C. Rixen, T. Jonas, G. Aberegg, and S. Wunderle (2008), Alpine grassland phenology as seen in AVHRR, VEGETATION, and MODIS NDVI time series—A comparison with in situ measurements, *Sensors*, *8*(4), 2833–2853.

Frankenberg, C., et al. (2011a), New global observations of the terrestrial carbon cycle from GOSAT: Patterns of plant fluorescence with gross primary productivity, *Geophys. Res. Lett.*, *38*, L17706, doi:10.1029/2011GL048738.

Frankenberg, C., A. Butz, and G. C. Toon (2011b), Disentangling chlorophyll fluorescence from atmospheric scattering effects in O2 A-band spectra of reflected sun-light, *Geophys. Res. Lett.*, *38*, L03801, doi:10.1029/2010GL045896.

Frankenberg, C., C. O'Dell, J. Berry, L. Guanter, J. Joiner, P. Köhler, R. Pollock, and T. E. Taylor (2014), Prospects for chlorophyll fluorescence remote sensing from the Orbiting Carbon Observatory-2, *Remote Sens. Environ.*, *147*, 1–12.

Goetz, S. J., A. G. Bunn, G. J. Fiske, and R. Houghton (2005), Satellite-observed photosynthetic trends across boreal North America associated with climate and fire disturbance, *Proc. Natl. Acad. Sci. U.S.A.*, *102*(38), 13,521–13,525.

Groendahl, L., T. Friborg, and H. Sogaard (2007), Temperature and snow-melt controls on interannual variability in carbon exchange in the high Arctic, *Theor. Appl. Climatol.*, *88*(1–2), 111–125.

Guanter, L., et al. (2014), Global and time-resolved monitoring of crop photosynthesis with chlorophyll fluorescence, *Proc. Natl. Acad. Sci. U.S.A.*, *111*(14), E1327–E1333.

Guanter, L., I. Aben, P. Tol, J. Krijger, A. Hollstein, P. Köhler, A. Damm, J. Joiner, C. Frankenberg, and J. Landgraf (2015), Potential of the TROPOspheric Monitoring Instrument (TROPOMI) onboard the Sentinel-5 Precursor for the monitoring of terrestrial chlorophyll fluorescence, *Atmos. Meas. Tech.*, *8*, 1337–1352.

Hall, D. K., G. A. Riggs, V. V. Salomonson, N. E. DiGirolamo, and K. J. Bayr (2002), MODIS snow-cover products, *Remote Sens. Environ.*, *83*(1), 181–194.

Henderson, J., et al. (2015), Atmospheric transport simulations in support of the Carbon in Arctic Reservoirs Vulnerability Experiment (CARVE), *Atmos. Chem. Phys.*, *15*(8), 4093–4116.

Hoffman, F. M., W. J. Riley, J. T. Randerson, S. M. Elliott, G. Keppel-Aleks, C. D. Koven, D. M. Lawrence, U. Mishra, J. K. Moore, and X. Yang (2015), Biogeochemistry-climate feedbacks: Quantifying feedbacks and uncertainties of biogeochemical processes in Earth System Models. paper presented at Regional and Global Climate Modeling (RGCM) Team Leads Meeting Hyatt Regency, Bethesda, Maryland, 6 Oct.

Huete, A., C. Justice, and W. Van Leeuwen (1999), *MODIS Vegetation Index (MOD13) Algorithm Theoretical Basis Document Version 3*, p. 213, Univ. of Arizona.

Jin, H., and L. Eklundh (2014), A physically based vegetation index for improved monitoring of plant phenology, *Remote Sens. Environ.*, *152*, 512–525.

Joiner, J., L. Guanter, R. Lindstrot, M. Voigt, A. Vasilkov, E. Middleton, K. Huemmrich, Y. Yoshida, and C. Frankenberg (2013), Global monitoring of terrestrial chlorophyll fluorescence from moderate-spectral-resolution near-infrared satellite measurements: Methodology, simulations, and application to GOME-2, *Atmos. Meas. Tech.*, *6*(10), 2803–2823.

Joiner, J., et al. (2014), The seasonal cycle of satellite chlorophyll fluorescence observations and its relationship to vegetation phenology and ecosystem atmosphere carbon exchange, *Remote Sens. Environ.*, *152*, 375–391.

Joiner, J., Y. Yoshida, L. Guanter, and E. M. Middleton (2016), New methods for retrieval of chlorophyll red fluorescence from hyper-spectral satellite instruments: Simulations and application to GOME-2 and SCIAMACHY, *Atmos. Meas. Tech.*, *9*, 3939–3967, doi:10.5194/amt-2015-387.

Jung, M., K. Henkel, M. Herold, and G. Churkina (2006), Exploiting synergies of global land cover products for carbon cycle modeling, *Remote Sens. Environ.*, *101*(4), 534–553.

Karion, A., C. Sweeney, S. Wolter, T. Newberger, H. Chen, A. Andrews, J. Kofler, D. Neff, and P. Tans (2013), Long-term greenhouse gas measurements from aircraft, *Atmos. Meas. Tech.*, *6*(3), 511–526.

Karion, A., et al. (2016), Investigating Alaskan methane and carbon dioxide fluxes using measurements from the CARVE tower, *Atmos. Chem. Phys.*, *16*(8), 5383–5398, doi:10.5194/acp-16-5383-2016.

Kwon, H.-J., W. C. Oechel, R. C. Zulueta, and S. J. Hastings (2006), Effects of climate variability on carbon sequestration among adjacent wet sedge tundra and moist tussock tundra ecosystems, *J. Geophys. Res.*, *111*, G03014, doi:10.1029/2005JG000036.

Larsen, K. S., A. Ibrom, S. Jonasson, A. Michelsen, and C. Beier (2007), Significance of cold-season respiration and photosynthesis in a subarctic heath ecosystem in Northern Sweden, *Global Change Biol.*, *13*(7), 1498–1508.

Lee, J.-E., et al. (2013), Forest productivity and water stress in Amazonia: Observations from GOSAT chlorophyll fluorescence, *Proc. R. Soc. B*, *280*(1761), 20130171.

Lin, J., C. Gerbig, S. Wofsy, A. Andrews, B. Daube, K. Davis, and C. Grainger (2003), A near-field tool for simulating the upstream influence of atmospheric observations: The stochastic time-inverted Lagrangian transport (STILT) model, *J. Geophys. Res.*, *108*(D16), 4493, doi:10.1029/2002JD003161.

Lipson, D. A., D. Zona, T. K. Raab, F. Bozzolo, M. Mauritz, and W. C. Oechel (2012), Water table height and microtopography control biogeochemical cycling in an Arctic coastal tundra ecosystem, *Biogeosciences*, *9*, 577–591.

Luus, K., and J. Lin (2015), The Polar Vegetation Photosynthesis and Respiration Model (PolarVPRM): A parsimonious, satellite data-driven model of high-latitude CO_2 exchange, *Geosci. Model Dev.*, *8*(2), 979–1027.

Luus, K., and J. Lin (2016), *CARVE Modeled Gross Ecosystem CO_2 Exchange and Respiration, Alaska, 2012–2014*, ORNL DAAC, Oak Ridge, Tennessee, doi:10.3334/ORNLDAAC/1314.

Luus, K., Y. Gel, J. Lin, R. Kelly, and C. Duguay (2013a), Pan-Arctic linkages between snow accumulation and growing-season air temperature, soil moisture and vegetation, *Biogeosciences*, *10*, 7575–7597.

Luus, K., R. Kelly, J. Lin, E. Humphreys, P. Lafleur, and W. Oechel (2013b), Modeling the influence of snow cover on low Arctic net ecosystem exchange, *Environ. Res. Lett.*, *8*(3), 035045.

Luus, K. A., J. C. Lin, R. E. Kelly, and C. R. Duguay (2013c), Subnivean Arctic and sub-Arctic net ecosystem exchange (NEE): Towards representing snow season processes in models of Nee using cryospheric remote sensing, *Prog. Phys. Geogr.*, *37*(4), 484–515.

Mahadevan, P., S. C. Wofsy, D. M. Matross, X. Xiao, A. L. Dunn, J. C. Lin, C. Gerbig, J. W. Munger, V. Y. Chow, and E. W. Gottlieb (2008), A satellite-based biosphere parameterization for net ecosystem CO_2 exchange: Vegetation Photosynthesis and Respiration Model (VPRM), *Global Biogeochem. Cycles*, *22*, GB2005, doi:10.1029/2006GB002735.

Mesinger, F., et al. (2006), North American regional reanalysis, *Bull. Am. Meteorol. Soc.*, *87*(3), 343–360.

Miller, C. E., and S. J. Dinardo (2012), CARVE: The Carbon in Arctic reservoirs vulnerability experiment. paper presented at 2012 IEEE Aerospace Conference, pp. 1–17, IEEE.

O'Sullivan, O. S., et al. (2016), Thermal limits of leaf metabolism across biomes, *Global Change Biol.*, *23*, 209–223, doi:10.1111/gcb.13477.

Parazoo, N. C., et al. (2013), Interpreting seasonal changes in the carbon balance of southern Amazonia using measurements of XCO_2 and chlorophyll fluorescence from GOSAT, *Geophys. Res. Lett.*, *40*, 2829–2833, doi:10.1002/grl.50452.

Pérez-Priego, O., et al. (2015), Sun-induced chlorophyll fluorescence and photochemical reflectance index improve remote-sensing gross primary production estimates under varying nutrient availability in a typical Mediterranean savanna ecosystem, *Biogeosciences*, *12*, 6351–6367.

Porcar-Castell, A., E. Tyystjärvi, J. Atherton, C. van der Tol, J. Flexas, E. E. Pfündel, J. Moreno, C. Frankenberg, and J. A. Berry (2014), Linking chlorophyll a fluorescence to photosynthesis for remote sensing applications: Mechanisms and challenges, *J. Exp. Bot.*, *65*, 4065–4095.

R Core Team (2013), *R: A Language and Environment for Statistical Computing*, R Found. for Stat. Comput., Vienna, Austria.

Roberts, D. A., S. L. Ustin, S. Ogunjemiyo, J. Greenberg, S. Z. Dobrowski, J. Chen, and T. M. Hinckley (2004), Spectral and structural measures of northwest forest vegetation at leaf to landscape scales, *Ecosystems*, *7*(5), 545–562.

Running, S. W., and M. Zhao (2015), *Daily GPP and Annual NPP (MOD17A2/A3) Products NASA Earth Observing System MODIS Land Algorithm*.

Schuur, E., et al. (2015), Climate change and the permafrost carbon feedback, *Nature*, *520*(7546), 171–179.

Schuur, E. A., et al. (2008), Vulnerability of permafrost carbon to climate change: Implications for the global carbon cycle, *BioScience*, *58*(8), 701–714.

Sims, D. A., et al. (2006), On the use of MODIS EVI to assess gross primary productivity of North American ecosystems, *J. Geophys. Res.*, *111*, G04015, doi:10.1029/2006JG000162.

Starr, G., and S. F. Oberbauer (2003), Photosynthesis of Arctic evergreens under snow: Implications for tundra ecosystem carbon balance, *Ecology*, *84*(6), 1415–1420.

Tarnocai, C., J. Canadell, E. Schuur, P. Kuhry, G. Mazhitova, and S. Zimov (2009), Soil organic carbon pools in the northern circumpolar permafrost region, *Global Biogeochem. Cycles*, *23*, GB2023, doi:10.1029/2008GB003327.

Tieszen, L. L. (1973), Photosynthesis and respiration in Arctic tundra grasses: Field light intensity and temperature responses, *Arct. Alp. Res.*, *5*, 239–251.

Walker, D. A., et al. (2005), The circumpolar Arctic vegetation map, *J. Veg. Sci.*, *16*(3), 267–282.

Walther, S., M. Voigt, T. Thum, A. Gonsamo, Y. Zhang, P. Koehler, M. Jung, A. Varlagin, and L. Guanter (2015), Satellite chlorophyll fluorescence measurements reveal large-scale decoupling of photosynthesis and greenness dynamics in boreal evergreen forests, *Global Change Biol.*, *22*, 2979–2996.

Wang, X., S. Piao, X. Xu, P. Ciais, N. MacBean, R. B. Myneni, and L. Li (2015), Has the advancing onset of spring vegetation green-up slowed down or changed abruptly over the last three decades?, *Global Ecol. Biogeogr.*, *24*(6), 621–631.

Wang, Z., C. Liu, and A. Huete (2002), From AVHRR-NDVI to MODIS-EVI: Advances in vegetation index research, *Acta Ecol. Sin.*, *23*(5), 979–987.

Yang, X., J. Tang, J. F. Mustard, J.-E. Lee, M. Rossini, J. Joiner, J. W. Munger, A. Kornfeld, and A. D. Richardson (2015), Solar-induced chlorophyll fluorescence that correlates with canopy photosynthesis on diurnal and seasonal scales in a temperate deciduous forest, *Geophys. Res. Lett.*, *42*, 2977–2987, doi:10.1002/2015GL063201.